Modulating Ion Diffusivity and Electrode Conductivity of Carbon Nanotube@Mesoporous Carbon Fibers for High Performance Aluminium-Selenium Batteries

Yueqi Kong, Ashok Kumar Nanjundan, Yang Liu, Hao Song, Xiaodan Huang and Chengzhong Yu**

Y. Q. Kong, Dr. A. K. Nanjundan, Dr. H. Song, Dr. X. D. Huang, Prof. C. Z. Yu

Australian Institute for Bioengineering and Nanotechnology, The University of Queensland, Brisbane QLD 4072, Australia
E-mail: x.huang@uq.edu.au; c.yu@uq.edu.au

Dr. Y. Liu, Prof. C. Z. Yu
School of Chemistry and Molecular Engineering, East China Normal University, Shanghai 200241, P. R. China

Keywords: rechargeable aluminium batteries, mesoporous carbon, selenium cathode, ion diffusivity, electrode conductivity

Abstract

Selenium (Se) based rechargeable aluminium batteries (RABs), known as aluminium-selenium (Al-Se) batteries, are an appealing new battery design that holds great promise for addressing the low-capacity problem of current RAB technology. However, their applications are hindered by mediocre high-rate capacity (~100 mAh g^{-1} at 0.5 A g^{-1}) and insufficient cycling life (50 cycles). Herein, we report the synthesis of mesoporous carbon fibers (MCFs) by coating mesoporous carbon with short-length mesopores and tunable mesopore sizes (2.7 to 8.9 nm) coaxially on carbon nanotubes (CNT). When compositing MCFs with Se for Al-Se batteries, a positive correlation between mesopore size and electrolyte ion diffusivity has been observed, however when pore size is increased to 8.9 nm, large voids are created at the interface of CNT core and mesoporous carbon shell, leading to decreased electrode conductivity. The trade-off between ion diffusivity and interfacial connectivity/conductivity determines MCF with pore size of 7.1 nm as the best host material for Al-Se batteries. The composite cathode delivers high specific capacities (366, 230 mAh g^{-1} at 0.5, 1 A g^{-1}), good rate performance and excellent cycling stability (152 mAh g^{-1} after 500 cycles at 2 A g^{-1}), superior over previously reported Se cathodes and other cathodes for RABs.

1. Introduction

Rechargeable aluminium batteries (RABs) are a promising new battery technology for future renewable energy storage, owing to the high capacity (2981mAh g^{-1}), rich natural abundance and good safety profile of Al.[1-5] Despite a number of pioneering studies on this battery technology, RABs still suffer from the low energy density because of the lack of high-performance cathodes.[2, 4] Currently, graphitic carbon materials are the most reported cathodes for RABs and have demonstrated attractive electrochemical performances of high voltage (>1.5 V), fast charge/discharge rate and exceptional cycling stability.[1-2, 6-8] However, state-of-the-art graphitic cathodes can only deliver limited specific capacities of ~60 to 150 mAh g^{-1}, due to their charge storage mechanism (intercalation/de-intercalation of bulky $AlCl_4^-$).[6-11] Other cathode materials including transition metal oxides,[12-13] dichalcogenides,[14-19] MXene,[20] and organic polymers/macrocyclic compounds[21-22] have also been investigated, nevertheless their performance including the specific capacity, discharge potential and cycling life remains to be improved.[23-24]

Recently, our group demonstrated the feasibility of utilizing Se as the active cathode component for RABs.[25] The working mechanism of Se cathode is mainly the reversible reaction of Se/Se_2Cl_2 redox pair with a high theoretical capacity of 339 mAh g^{-1}. This new battery design (denoted as Al-Se batteries) consists of a composite cathode containing Se nanorods and mesoporous carbon (CMK-3), an Al metal anode and chloroaluminate ionic liquid electrolyte, in which mesoporous carbon has a critical role of both trapping liquid Se_2Cl_2 and providing conductive host to facilitate electrochemical reactions. Assisted by CMK-3 mesoporous carbon, Se cathode delivered a reversible capacity of 178 mAh g^{-1} at 100 mA g^{-1} with a discharge voltage above 1.5 V. However, this capacity is only around half of the theoretical value and decays rapidly at a high current rate (101 mAh g^{-1} at 500 mA g^{-1}). The cycling stability is also far from satisfactory, showing just 50 charge/discharge cycles. These

moderate electrochemical performances could be largely attributed to the small pore size (3.4 nm) and long channel-like (>1 μm) pore geometry of CMK-3 which are unfavourable for the bulky electrolyte ions ($AlCl_4^-$, ~0.53 nm; $Al_2Cl_7^-$, ~0.93 nm) transporting and/or reacting with Se_2Cl_2 species (~0.67 nm).[1, 26] Therefore, rational design of host materials holds the key for the development of Al-Se batteries with high performance.

In the research and development of rechargeable battery technologies, mesoporous carbon materials have made remarkable contributions, due to their high ability to adsorb and interact with active species at both electrodes and electrolytes.[27-29] Among various mesoporous carbons applied in different battery systems, mesoporous carbon nanofibers have attracted particular interest.[27, 30-32] This type of materials usually has a typical core-shell structure composed of a carbon nanotube (CNT) core and amorphous mesoporous carbon shell, which can synergistically facilitate the dynamic electrochemical processes/reactions at electrolyte/electrode interfaces by providing short-length carbon mesopores and improved electrical conductivity.[30-32] Several core-shell structured mesoporous carbon fibers have been prepared by either replication of mesoporous silica[31, 33-34] or soft-templating methods.[32] They were applied as host materials for sulfur[30-31, 34] or tellurium[35] in rechargeable lithium batteries and demonstrated improved electrochemical properties. However, in previous reports usually mesoporous carbon with one given pore size is coated on CNT, there are rare reports of mesoporous carbon fiber materials with tunable mesopore sizes in one study.[31-34] It has been reported that the size of mesopores is critical in determining the ion/electrolyte transport property.[36] Moreover, the mesopore size could affect the interfacial connection between the amorphous mesoporous carbon shell and CNT core, consequently the electrical conductivity and electrochemical performance. To our knowledge, there is a gap in understanding the fundamental relationship between mesopore size and conductivity/diffusivity of CNT@mesoporous carbon based materials.

Herein, we report mesoporous carbon fibers (MCFs) with finely controllable pore structures as excellent materials for Al-Se batteries with high performance. MCFs were synthesized through an interfacial cooperative assembly of resorcinol-formaldehyde (RF) resin and *in-situ* formed silica primary particle clusters on CNTs (Figure S1). After calcination and silica removal, MCFs with high specific surface area (733 to 941 m^2 g^{-1}) and large pore volume (0.90 to 1.53 cm^3 g^{-1}) can be obtained. By simply adjusting the silica precursor content, the mesopore size of MCFs can be finely tuned (2.7, 5.0, 7.1 and 8.9 nm) with a controlled mesoporous carbon-CNT connectivity. The influences of structural modulation on electrochemical properties were evaluated in Al-Se batteries by compositing MCFs with Se nanorods (MCFs/Se) as cathodes (**Figure 1a**). It is demonstrated that the diffusivity of the chloroaluminate anions increases with the mesopore size increasing, however expanding the mesopore size to 8.9 nm leads to irregular large voids and discontinued mesoporous carbon-CNT connection, which is detrimental to the conductivity and battery performances (Figure 1b). Therefore, MCF-7 with a compromised large pore size (7.1 nm) and intimate mesoporous carbon-CNT connectivity can induce the best cathode performance among the four MCFs under test. A high reversible capacity of 230 mAh g^{-1} at 1A g^{-1} after 100 cycles and exceptional rate/long-cycling stabilities (152 mAh g^{-1} after 500 cycles at 2 A g^{-1}) are obtained, superior over the previously reported Se cathode and other cathode materials used in RABs (Table S1).[1, 6-10, 13-25] Our contribution has provided new knowledge in understanding the mesopore size and conductivity/diffusivity relationship for the rational design of electrochemical systems with improved performance.

2. Results and Discussion

MCF materials with tunable mesopore size and controlled core-shell connectivity were prepared through varying the TEOS amount in a cooperative assembly system containing RF precursors and CNTs (Figure S1). With the assist of ammonia catalyst, silica primary particles were derived from TEOS and co-deposited with RF resin on CNT surface. By increasing the TEOS amount from 50 to 200

μL while keeping CNT and RF amount constant, the silica primary particle concentration increases in the suspension, resulting in a size growing of silica clusters deposited on CNTs. The followed carbonization and silica etching converted RF to amorphous carbon and created mesopores with tunable structure. The final products are denoted as MCF-x, where x refers to the approximate mesopore size.

The morphology and mesoporous structure of MCFs were characterized by SEM and TEM. A clear fibrous morphology can be observed in the low-magnification SEM images of four MCF materials (Figure S2 a-h). These fibers have high aspect ratios with general lengths of several microns and relatively narrow diameters. The diameters of MCFs are quite uniform with sizes of ~100 nm estimated from high-magnification SEM images in **Figure 2** a-d. CNTs can be also observed at the pointy ends of some fibers particularly in MCF-7 (Figure 2c, indicated by arrows), indicating a coaxial core-shell structure. Such structural features can be more clearly observed in TEM and ET characterizations. TEM images of MCF single fibers reveal well-defined core-shell structure with clear boundaries between CNTs and amorphous carbon shells (Figure 2 e-h). Comparing with pristine CNTs (Figure S3), MCFs well maintain the one-dimensional fibrous morphology with relatively uniform mesoporous carbon coatings of ~30 nm thickness. Mesopores of short pore lengths can be identified by the contrast difference in shell layers and show increasing pore sizes from Figure 2 e to h.

The inter-connectivity between mesoporous carbon shell and CNT core is difficult to be revealed by conventional TEM observation. An ET technique was employed to characterize this structure information of MCFs. A series of tilted images were recorded in the range from −65° to +65° and processed using IMOD software (see material characterizations).[36-39] The ET slices that cut from the middle of MCF fibers are shown in Figure 2 i-l. It is demonstrated that the mesopores in MCF-3, MCF-

5 and MCF-7 are quite evenly distributed in amorphous carbon shells, enabling closely connected core-shell architectures. However, in the case of MCF-9, CNT and carbon shell are largely separated by irregular voids (Figure 2l, indicated by arrows), which weakens the core-shell connectivity in this material. Such structural difference can be ascribed to the Volmer-Weber growth mode (island formation) for silica deposition on graphitic carbonaceous surfaces[36] and the variation of TEOS amount in cooperative assembly steps.[38-39] At 50-150 µL TEOS amount, the polymerization rate of TEOS and RF can be well matched by giving a 3 hours interval time, creating uniform silica/RF assemblies and thus evenly distributed mesopores. Further increasing TEOS content to 200 µL accelerates the silica polymerization and causes pre-deposition of large silica aggregates on CNTs, which eventually leads to a separated core-shell structure.

Nitrogen adsorption/desorption measurements were conducted to quantitatively characterize the mesopore structure parameters of MCF materials. As shown in Figure 2m, the nitrogen adsorption isotherms of four MCFs demonstrate typical type-IV profiles with hysteresis loops indicating meso-porosity in carbon shells. Analysed from the isotherms, MCF materials have high surface areas of 941, 848, 733, 749 $m^2 g^{-1}$, and large pore volume of 1.53, 1.24, 0.91, 0.90 $cm^3 g^{-1}$ (Table S2). The mesopore size distributions calculated from adsorption branches using BJH method display relatively broad peaks centred at 2.7, 5.0, 7.1 and 8.9 nm for MCF-3, MCF-5, MCF-7 and MCF-9 (Figure 2n), respectively, demonstrating an effective mesopore size control.

To evaluate the influence of mesoporous structure on the electrical property of MCFs, the direct current (DC) electrical conductivity of four MCFs were measured (Table S3) and compared with pristine CNTs and pure mesoporous carbon without CNT core (denoted as MC-7, ~7.4 nm pore size, see Figure S4). In comparison to MC-7 (0.81 S cm^{-1}), the incorporation of CNTs (6.35 S cm^{-1}) clearly improved the overall electrical conductivity of MCFs. The conductivity was found to be highest for

MCF-3 (1.54 S cm^{-1}) and then gradually declined with pore size increasing (1.27 and 1.17 S cm^{-1} for MCF-5 and MCF-7, respectively). When the mesopore size was enlarged to 8.9 nm (MCF-9), the electrical conductivity dropped to 0.90 S cm^{-1}, approaching to the value of pure mesoporous carbon, which indicates that large mesopore might be detrimental to the conductivity.

The application of MCF materials in Al-Se batteries were demonstrated by compositing MCFs with Se nanorods as cathodes (MCFs/Se). Trigonal Se nanorods were prepared using a reported protocol[25] (Figure S5), and then physically mixed with MCFs in the weight ratio of 2:1 to form MCFs/Se composites. Accordingly, the Se content was calculated to be 66.7 wt% for each MCF/Se composite. The MCFs/Se composites are cast onto carbon cloth substrates with carbon black and Nafion binder (weight ratio 7:2:1) to prepare cathodes. These cathodes were assembled into corrosion resistant coin-cell cases and tested by galvanostatic charge/discharge measurements. Typical charge/discharge profiles of MCFs/Se cathodes at 1 A g^{-1} are presented in **Figure 3** a-d. The MCFs/Se cathodes present high charge and discharge voltage plateaus at ~2.0-2.3 V and ~1.9-1.5 V, respectively, and show no obvious polarization over 100 cycles. Among four MCFs/Se cathodes, MCF-7/Se exhibits the highest initial discharge capacity of 299 mAh g^{-1} at 1 A g^{-1} and maintain well after 100 cycles (230 mAh g^{-1}, Figure 3e), which is superior than the previously reported Se cathode and other cathode materials applied in RABs (Table S1).[1, 6-10, 13-25] The initial discharge capacities of MCF-9/Se, MCF-5/Se and MCF-3/Se at 1 A g^{-1} are 213, 211 and 163 mAh g^{-1}, and can be maintained at 183, 193 and 169 mAh g^{-1} after 100 charge/discharge cycles. The capacity difference of MCF-3/Se and MCF-5/Se suggests that small mesopores are detrimental to the cathode performance, as MCF-3 and MCF-5 have very similar other pore parameters (Table S2). The significant capacity improving in MCF-7/Se over MCF-3/Se and MCF-5/Se can be attributed to its larger mesopore size and higher porosity that facilitate both Se_2Cl_2 adsorption and ion/electrolyte transport. However, despite the

even higher pore size and porosity, MCF-9 can only deliver inferior performances owing to its separated core-shell structure and the consequent inadequate electrical conductivity.

In order to understand the electrochemical processes of MCFs/Se cathodes during battery cycling, their morphology and chemical composition were monitored by *ex-situ* electron microscopy and XPS analyses. Before battery cycling, the SEM image of a typical MCF-7/Se cathode shows a uniform mixture of Se nanorods and agglomerated MCF-7 fibers (Figure S6 a and b). The Se nanorods in cathode are relatively shorter than pristine Se (Figure S5), which may be due to the vigorous grinding processes in preparing MCFs/Se mixture and composite cathodes. These short Se nanorods are nearly all disappeared after the first cycle at 1 A g^{-1} leaving only MCF-7 (Figure S6 c and d), suggesting a complete Se/Se_2Cl_2 reaction confined within MCF-7 mesopores (Figure 1a). The confinement of Se redox reactions can be further elucidated by the corresponding TEM analysis during battery cycling at 1 A g^{-1}. Before battery operation, the TEM elemental mapping results of a typical MCF-7/Se cathode show a co-existence but separated feature of short Se nanorods and carbon fibers (**Figure 4** a-c). After finishing a charge/discharge cycle (Figure 4 d-f), only carbon fibers can be observed with Se absorbed in their mesopores, which confirms the MCF-7's role of capturing liquid Se_2Cl_2 and hosting Se/Se_2Cl_2 redox reactions in carbon mesopores (Figure 1a). Such Se adsorbed carbon mesopore feature was well retained after 100 cycles cell operating (Figure 4 g-i), indicating a stable MCF-7/Se cathode design. The adsorption of Se species into carbon mesopores can also be validated by the nitrogen adsorption/desorption analysis of MCF-7/Se cathode (Figure S7). The mesopores in fresh MCF-7/Se cathode completely disappeared after 100 cycles, proving the role of carbon mesopores for hosting Se/Se_2Cl_2 redox reactions.

The chemical state and composition changes of MCFs/Se cathode during Al-Se battery cycling were investigated by XPS analysis (Figure 4 j and k). In the typical MCF-7/Se cathode, it is

demonstrated that the Se 3d peak shifts from 55.0 eV to 55.9 eV after a complete charge/discharge cycle at 1 A g^{-1} and maintains at 56.0 eV for 100 cycles (Figure 4 j), indicating the transformation of initial trigonal Se to amorphous Se during Al-Se battery working, which is consistent with our previous report.[25] More importantly, the relative Se content (Se to carbon ratio) changes of MCFs/Se cathodes during battery cycling have been also analysed (Figure 4 k). Comparing four MCFs/Se cathodes, MCF-7/Se and MCF-9/Se showed much higher Se retentions than MCF-3/Se and MCF-5/Se after the first cycle at 1 A g^{-1}, because of their higher porosity for Se_2Cl_2 capture. The relatively lower Se content in MCF-9/Se than MCF-7/Se in the first cycle implies more Se_2Cl_2 leaching from MCF-9 mesopores due to inefficient Se_2Cl_2/Se redox conversion, which can explain the low initial capacity of MCF-9/Se cathode. The Se_2Cl_2 leaching in both MCF-7/Se and MCF-9/Se cathodes gradually accumulated over 100 cycles and resulted in discharge capacity decay. Nevertheless, MCF-7/Se cathode maintianed much higher Se content and capacity retention than MCF-9/Se, demonstrating its advantageous mesoporous structure for stablizing Se cathode.

The rate capacity and long cycling stability of MCFs/Se cathodes were evaluated by testing them at different current densities. **Figure 5** a and b are typical charge/discharge profiles of each cathode at 0.5 and 2 A g^{-1}, which show quite similar charge and discharge voltage plateaus to the curves at 1 A g^{-1} (Figure 3 a-d). The relatively shortened charge and discharge plateaus at 2 A g^{-1} can be attributed to the slight polarization caused by the high charge/discharge rate. The rate capacities of MCFs/Se cathodes at 0.5, 1 and 2 A g^{-1}, are shown in Figure 5c. At 0.5 A g^{-1}, MCF-9/Se, MCF-7/Se, MCF-5/Se and MCF-3/Se can achieve high specific discharge capacity of 354, 366, 233 and 220 mAh g^{-1}, respectively. The high capacity over the theoretical value could be caused by the partial oxidation of Se^0 to high valance Se species (e.g. Se^{2+}, Se^{4+}).[40-41] At 1 A g^{-1}, the rate performance measurements show very similar discharge capacities to those in 1 A g^{-1} cycling tests, demonstrating a good battery consistence. When increasing the current to a high rate of 2 A g^{-1}, MCF-7/Se cathode can still

maintain a high capacity of 155 mAh g^{-1}, which is much higher than the capacity of other MCFs/Se cathodes (129, 85, 69 mAh g^{-1} for MCF-9/Se, MCF-5/Se, MCF-3/Se) and previously reported RAB cathodes at this current (Table S1).[1-2, 6-9, 23-24] Furthermore, long cycling tests were conducted at the high current rate of 2 A g^{-1} to demonstrate the cycling stabilities of MCFs/Se cathodes. As shown in Figure 5d, all four MCFs/Se cathodes exhibit exceptional cycling stability with negligible capacity decay over long-term testing and MCF-7/Se demonstrates the highest reversible capacity of 152 mAh g^{-1} after 500 cycles.

The electrochemical kinetics of MCFs/Se cathodes in Al-Se batteries were investigated by cyclic voltammetry (CV) and electrochemical impedance spectroscopy (EIS) analyses to elucidate their exceptional high rate performance. The CV scanning curves of a typical MCF-7/Se cathode (**Figure 6a**) show anodic peaks at ~2.1-2.2 V and cathodic peaks at ~1.5-1.7 V, corresponding to Se^0 oxidation and Se_2Cl_2 reduction, respectively. The CV scanning results (peak current i and scan rate v) were analysed using the power law equation (Equation 1):

$$i = a \times v^b \quad (1)$$

in which a and b are adjustable parameters. The b parameter, determined by log(i) to log(v) slope, is the key factor to indicate the amount of capacity contribution by diffusion faradaic process (b = 0.5) and capacitive process (fast surface faradaic charge-transfer, b = 1).[42-44] Comparing to previously reported CMK-3/Se cathode (b_{anodic}: 0.48, $b_{cathodic}$: 0.54), MCF-7/Se shows increased anodic and cathodic b values of 0.60 and 0.67 (Figure 6b), suggesting a combination of both diffusion and capacitive capacity contributions.[42, 44] Such electrochemical behaviours could be ascribed to its short-length mesopore and relatively large pore size that stimulate the ion/electrolyte transport and enable rapid electrochemical redox reactions.

The capacity contribution from diffusion process and capacitive process at a fixed scan rate can be quantitatively differentiated based on their dependence on the scan rate (capacitive contribution: $k_1 \times v$, diffusion contribution: $k_2 \times v^{1/2}$) in Equation 2:[42, 45-46]

$$i(v) = k_1 \times v + k_2 \times v^{1/2} \quad (2)$$

The constants k_1 and k_2 can be determined by plotting $i(v)/v^{1/2}$ against $v^{1/2}$, which will allow to quantify the capacitive and diffusion contributions (Figure 6c). The capacity contribution ratios of these two processes for MCFs/Se cathodes at different scan rates are summarized in Figure 6d. In general, the diffusion capacity dominates more than half of total capacity in all tested cathodes. The capacitive contribution increases with the rising of scan rate in four MCFs/Se cathodes, which explains their improved electrochemical performances compared to CMK-3/Se cathode and validates the advantage of fibrous mesoporous carbon structure. The importance of large mesopore size can also be reflected in this analysis, since MCF-9/Se and MCF-7/Se display higher capacitive contribution ratios than MCF-5/Se and MCF-3/Se.

To quantitatively evaluate the ion diffusivity and electrochemical conductivity of MCFs/Se cathodes in Al-Se batteries, their EIS spectra were measured and analysed (Figure 6e and Figure S8). Figure 6e shows the Nyquist plot and the fitted equivalent circuit diagram of MCF-7/Se. The low frequency region of the Nyquist plot exhibits a typical linear feature, providing information on the diffusion resistance encountered by electrolyte ions transportation at the electrode, also known as the Warburg impedance.[36, 47-48] By plotting measured resistance results against the inverse square root of frequency (Figure S8 d), the Warburg factors (σ) can be obtained, thus allowing calculation of ion diffusion coefficients (D). Diffusion coefficients are found to be highest for MCF-9/Se with a value of 7.75×10^{-8} cm^2 s^{-1} and gradually decline to 2.36×10^{-8} cm^2 s^{-1} for MCF-3/Se (Table S4), indicating the reduced ion diffusivity by mesopore size decreasing (Figure 1b).

In the high frequency region of the Nyquist plots (Figure 6e and Figure S8 a-c), the diameters of the semicircles are correlated to the charge transfer resistance (R_{ct}).[36, 47] Comparing R_{ct} values of the four cathodes (Figure 6f, Table S4), MCF-3/Se and MCF-5/Se have near-equally high R_{ct} (15.26 and 15.36 Ω), further proving the detriment of small mesopores to both electrolyte ion transport and the subsequent faradaic processes, which is consistent with the ion diffusivity analysis. More importantly, the R_{ct} comparison between MCF-7/Se and MCF-9/Se reflects an opposite trend to their ion diffusion coefficients and shows an increased resistance in larger mesopore material (11.4 Ω > 6.33 Ω, Table S4). This result confirms the importance of the intimate connectivity between mesoporous carbon shell and CNT core for improving electrical conductivity and reducing electrochemical resistance in Al-Se battery operations (Figure 1b). Therefore, MCF-7 with the compromised structure of large mesopore size and close core-shell interconnection can assist the composite Se cathode to deliver superior performances in Al-Se batteries.

3. Conclusion

In summary, MCFs with high meso-porosity and controllable pore structures have been prepared and applied in Al-Se batteries to assess the impact of their structural parameters on Se cathode performances. Based on material characterisations, battery performance tests and electrochemical kinetics analyses, it is demonstrated that the chloroaluminate ion diffusivity in composite Se cathodes is positively correlated to the mesopore size, while an intimate connectivity between mesoporous carbon shell and CNT core plays a critical role in improving the electrical conductivity of a composite cathode. Rationally design fibrous mesoporous carbon structures with large mesopore size and close core-shell connection can greatly facilitate the electrolyte ion transportation and charge transfers during battery redox reaction, and consequently promote the performances of Se cathodes in Al-Se batteries. These findings and the novel materials provide new inspirations for the

development of high performance RAB technologies, and have the potential to be applied in other rechargeable battery systems.

4. Experimental Section

Material synthesis: In a typical synthesis procedure, multiwall CNTs (40 mg) were dispersed into a water/ethanol (6/36 mL) solution containing ammonium hydroxide solution (1.4 mL, 28 wt%) under ultrasonication and stirring. Resorcinol (125 mg), formaldehyde solution (250 µL, 37 wt%) and ethylenediamine (50 µL) were added into the solution and stirred at room temperature for 3 hours. Then, tetraethyl orthosilicate (TEOS) (50-200 µL) was added and the mixture was kept stirring for another 5 hours followed by centrifugation at 4700 rpm to obtain precipitates. The precipitates were rinsed three times in water/ethanol (1:1 v/v) solution before drying overnight at 80 °Cin vacuum ovens. The dried precipitates were carbonized at 700 °Cfor 4 hours in argon. Finally, MCFs were obtained after silica etching (hydrofluoric acid, 10 wt%, 24 hours) and drying (80 °Cin vacuum ovens).

Electrochemical measurements: Se nanorods synthesized by a reported method[25] were grinded with MCFs at a weight ratio of 2:1 to obtain the composite. The composite was mixed with carbon black and Nafion binder in n-methylpyrrolidone at a weight ratio of 7:2:1 to form the electrode slurry. The slurry was casted on carbon cloth substrates and dried overnight at 80 °Cin a vacuum oven to obtain the cathodes. The specific Se loading on each cathode was about 2.5-3 mg cm^{-2}. Al-Se batteries were assembled in an Argon-filled glovebox in poly (3,4-ethylenedioxythiophene) coated coin cell cases (CR2032) using pure Al foil as anodes, 1-ethyl-3-methylimidazolium chloride-aluminum chloride ($EMImCl/AlCl_3$, 1: 1.1 by mole) as electrolytes and glass fiber (Filtech) as separators. Galvanostatic charge/discharge measurements were performed on Land battery testers in the voltage range between 1.0 to 2.3V. The specific charge and discharge capacities are all calculated by the mass of

Se. The Cyclic voltammetry (CV), and electrochemical impedance spectroscopy (EIS) analyses were conducted on a Solartron-Multistat electrochemical workstation.

Material characterizations: The morphology and mesopore structure of MCF materials were characterized by transmission electron microscope (TEM, Hitachi HT7700) at 120 kV and field emission scanning electron microscope (FESEM, JEOL 7800) operated at 1 kV. Electron tomography (ET) was conducted with a FEI Tecnai F30 TEM. Samples were deposited onto Formvar film of copper grids. Gold nanodots (~10 nm) were deposited on both sides of the grid as fiducial markers. TEM images were digitally recorded at a given defocus in the range −65° to +65° with increment of 1°. Data processing was performed by IMOD software. Nitrogen adsorption/desorption measurements were conducted using a Micromeritics Tristar ⅡSurface Area and Porosity analyser. Before analysis, MCF samples were degassed at 200 ℃for 12 hours. The surface area was calculated by Brunauer-Emmett-Teller (BET) method using adsorption data at a relative pressure (P/P_0) range from 0.05 to 0.25. The pore size distribution was determined by Barrett-Joyner-Halenda (BJH) method using the adsorption branch. The total pore volume was estimated from the amount nitrogen adsorbed at the highest P/P_0 (0.99). X-ray diffraction (XRD) pattern was obtained using a Brucker X-ray Diffractometer (D8 Advance, λ=1.5406Å). Raman spectroscopy measurement was conducted on a Renishaw Raman spectrometer using Argon laser (wavelength at 514nm). X-ray photoelectron spectroscopy (XPS) results were obtained from a Kratos Axis ULTRA X-ray photoelectron spectrometer. The atomic concentration calculation and peak fitting were calculated by the Casa XPS version 2.3.14 software.

Supporting Information

Supporting Information is available from the Wiley Online Library or from the author.

Acknowledgements

We acknowledge the financial support from Australian Research Council, Queensland Government, China Scholarship Council and the University of Queensland. We also thank Australian National Fabrication Facility, Australian Microscopy and Microanalysis Research Facility at the Centre for Microscopy and Microanalysis, the University of Queensland for technical assistance.

Received: ((will be filled in by the editorial staff))
Revised: ((will be filled in by the editorial staff))
Published online: ((will be filled in by the editorial staff))

References

[1] M. C. Lin, M. Gong, B. G. Lu, Y. P. Wu, D. Y. Wang, M. Y. Guan, M. Angell, C. X. Chen, J. Yang, B. J. Hwang, H. J. Dai, *Nature*, **2015**, *520*, 325.

[2] S. K. Das, *Angew. Chem. Int. Ed.*, **2018**, *57*, 16606.

[3] F. Ambroz, T. J. Macdonald, T. Nann, *Adv. Energy Mater.*, **2017**, *7*, 1602093.

[4] F. Wu, H. Y. Yang, Y. Bai, C. Wu, *Adv. Mater.*, **2019**, *31*, 1806510.

[5] G. A. Elia, K. Marquardt, K. Hoeppner, S. Fantini, R. Y. Lin, E. Knipping, W. Peters, J. F. Drillet, S. Passerini, R. Hahn, *Adv. Mater.*, **2016**, *28*, 7564.

[6] H. Chen, H. Y. Xu, S. Y. Wang, T. Q. Huang, J. B. Xi, S. Y. Cai, F. Guo, Z. Xu, W. W. Gao, C. Gao, *Sci. Adv.*, **2017**, *3*, eaao7233.

[7] H. Chen, F. Guo, Y. J. Liu, T. Q. Huang, B. N. Zheng, N. Ananth, Z. Xu, W. W. Gao, C. Gao, *Adv. Mater.*, **2017**, *29*, 1605958.

[8] X. Z. Yu, B. Wang, D. C. Gong, Z. Xu, B. G. Lu, *Adv. Mater.*, **2017**, *29*, 1604118.

[9] Z. M. Liu, J. Wang, H. B. Ding, S. H. Chen, X. Z. Yu, B. A. Lu, *ACS Nano*, **2018**, *12*, 8456.

[10] H. B. Sun, W. Wang, Z. J. Yu, Y. Yuan, S. Wang, S. Q. Jiao, *Chem. Commun.*, **2015**, *51*, 11892.

[11] X. D. Huang, Y. Liu, H. W. Zhang, J. Zhang, O. Noonan, C. Z. Yu, *J. Mater. Chem. A*, **2017**, *5*, 19416.

[12] J. G. Tu, H. P. Lei, Z. J. Yu, S. Q. Jiao, *Chem. Commun.*, **2018**, *54*, 1343.

[13] X. F. Zhang, G. H. Zhang, S. Wang, S. J. Li, S. Q. Jiao, *J. Mater. Chem. A*, **2018**, *6*, 3084.

[14] S. Wang, S. Q. Jiao, J. X. Wang, H. S. Chen, D. H. Tian, H. P. Lei, D. N. Fang, *ACS Nano*, **2017**, *11*, 469.

[15] S. Wang, Z. J. Yu, J. G. Tu, J. X. Wang, D. H. Tian, Y. J. Liu, S. Q. Jiao, *Adv. Energy Mater.*, **2016**, *6*, 1600137.

[16] Z. J. Yu, Z. P. Kang, Z. Q. Hu, J. H. Lu, Z. Zhou, S. Q. Jiao, *Chem. Commun.*, **2016**, *52*, 10427.

[17] T. H. Cai, L. M. Zhao, H. Y. Hu, T. G. Li, X. C. Li, S. Guo, Y. P. Li, Q. Z. Xue, W. Xing, Z. F. Yan, L. Z. Wang, *Energy Environ. Sci.*, **2018**, *11*, 2341.

[18] Y. X. Hu, B. Luo, D. L. Ye, X. B. Zhu, M. Q. Lyu, L. Z. Wang, *Adv. Mater.*, **2017**, *29*, 1606132.

[19] Y. X. Hu, D. L. Ye, B. Luo, H. Hu, X. B. Zhu, S. C. Wang, L. L. Li, S. J. Peng, L. Z. Wang, *Adv. Mater.*, **2018**, *30*, 1703824.

[20] A. VahidMohammadi, A. Hadjikhani, S. Shahbazmohamadi, M. Beidaghi, *ACS Nano*, **2017**, *11*, 11135.

[21] M. Walter, K. V. Kravchyk, C. Bofer, R. Widmer, M. V. Kovalenko, *Adv. Mater.*, **2018**, *30*, 1705644.

[22] D. J. Kim, D. J. Yoo, M. T. Otley, A. Prokofjevs, C. Pezzato, M. Owczarek, S. J. Lee, J. W. Choi, J. F. Stoddart, *Nat. Energy*, **2019**, *4*, 51.

[23] N. P. Stadie, S. T. Wang, K. V. Kraychyk, M. V. Kovalenko, *ACS Nano*, **2017**, *11*, 1911.

[24] C. X. Li, S. H. Dong, R. Tang, X. L. Ge, Z. W. Zhang, C. X. Wang, Y. P. Lu, L. W.Yin, *Energy Environ. Sci.*, **2018**, *11*, 3201.

[25] X. D. Huang, Y. Liu, C. Liu, J. Zhang, O. Noonan, C. Z. Yu, *Chem. Sci.*, **2018**, *9*, 5178.

[26] Z. Akdeniz, G. Pastore, M. P. Tosi, *Phys. Chem. Liq.*, **1996**, *32*, 191.

[27] W. Li, J. Liu, D. Y. Zhao, *Nat. Rev. Mater.*, **2016**, *1*, doi: doi.org/10.1038/natrevmats.2016.23.

[28] W. Li, Q. Yue, Y. H. Deng, D. Y. Zhao, *Adv. Mater.*, **2013**, *25*, 5129.

[29] L. Peng, C. T. Hung, S. W. Wang, X. M. Zhang, X. H. Zhu, Z. W. Zhao, C. Y. Wang, Y. Tang, W. Li, D. Y. Zhao, *J. Am. Chem. Soc.*, **2019**, *141*, 7073.

[30] S. Xin, L. Gu, N. H. Zhao, Y. X. Yin, L. J. Zhou, Y. G. Guo, L. J. Wan, *J. Am. Chem. Soc.*, **2012**, *134*, 18510.

[31] Y. Zhao, W. L. Wu, J. X. Li, Z. C. Xu, L. H. Guan, *Adv. Mater.*, **2014**, *26*, 5113.

[32] X. H. Zhu, Y. Xia, X. M. Zhang, A. A. Al-Khalaf, T. C. Zhao, J. X. Xu, L. Peng, W. N. Hozzein, W. Li, D. Y. Zhao, *J. Mater. Chem. A*, **2019**, *7*, 8975.

[33] X. F. Qian, Y. Y. Lv, W. Li, Y. Y. Xia, D. Y. Zhao, *J. Mater. Chem.*, **2011**, *21*, 13025.

[34] D. L. Wang, Y. C. Yu, W. D. Zhou, H. Chen, F. J. DiSalvo, D. A. Muller, H. D. Abruna, *Phys. Chem. Chem. Phys.*, **2013**, *15*, 9051.

[35] J. Zhang, Y. X. Yin, Y. You, Y. Yan, Y. G. Guo, *Energy Tech.*, **2014**, *2*, 757.

[36] Y. Liu, H. W. Zhang, H. Song, O. Noonan, C. H. Lang, X. D. Huang, C. Z. Yu, *J. Phys. Chem. C*, **2017**, *121*, 23947.

[37] X. D. Huang, K. Qian, J. Yang, J. Zhang, L. Li, C. Z. Yu, D. Y. Zhao, *Adv. Mater.*, **2012**, *24*, 4419.

[38] H. W. Zhang, M. H. Yu, H. Song, O. Noonan, J. Zhang, Y. N. Yang, L. Zhou, C. Z. Yu, *Chem. Mater.*, **2015**, *27*, 6297.

[39] H. W. Zhang, O. Noonan, X. D. Huang, Y. N. Yang, C. Xu, L. Zhou, C. Z. Yu, *ACS Nano*, **2016**, *10*, 4579.

[40] J. Robinson, R. A. Osteryoung, *J. Electrochem. Soc.*, **1978**, *125*, 1454.

[41] M. Matsunaga, M. Morimitsu, K. Hosokawa, *J. Electrochem. Soc.*, **1995**, *142*, 2910.

[42] D. W. Su, K. Kretschmer, G. X. Wang, *Adv. Energy Mater.*, **2016**, *6*, 1501785.

[43] H. Lindstrom, S. Sodergren, A. Solbrand, H. Rensmo, J. Hjelm, A. Hagfeldt, S. E. Lindquist, *J. Phys. Chem. B*, **1997**, *101*, 7717.

[44] P. Simon, Y. Gogotsi, B. Dunn, *Science*, **2014**, *343*, 1210.

[45] Y. L. Wu, X. Fan, R. R. Gaddam, Q. L. Zhao, D. F. Yang, X. M. Sun, C. Wang, X. S. Zhao, *J. Power Sources*, **2018**, *408*, 82.

[46] T. C. Liu, W. G. Pell, B. E. Conway, S. L. Roberson, *J. Electrochem. Soc.*, **1998**, *145*, 1882.

[47] O. Noonan, Y. Liu, X. D. Huang, C. Z. Yu, *J. Mater. Chem. A*, **2018**, *6*, 14272.

[48] H. W. Chen, C. H. Wang, Y. F. Dai, S. Q. Qiu, J. L. Yang, W. Lu, L. W. Chen, *Nano Lett.*, **2015**, *15*, 5443.

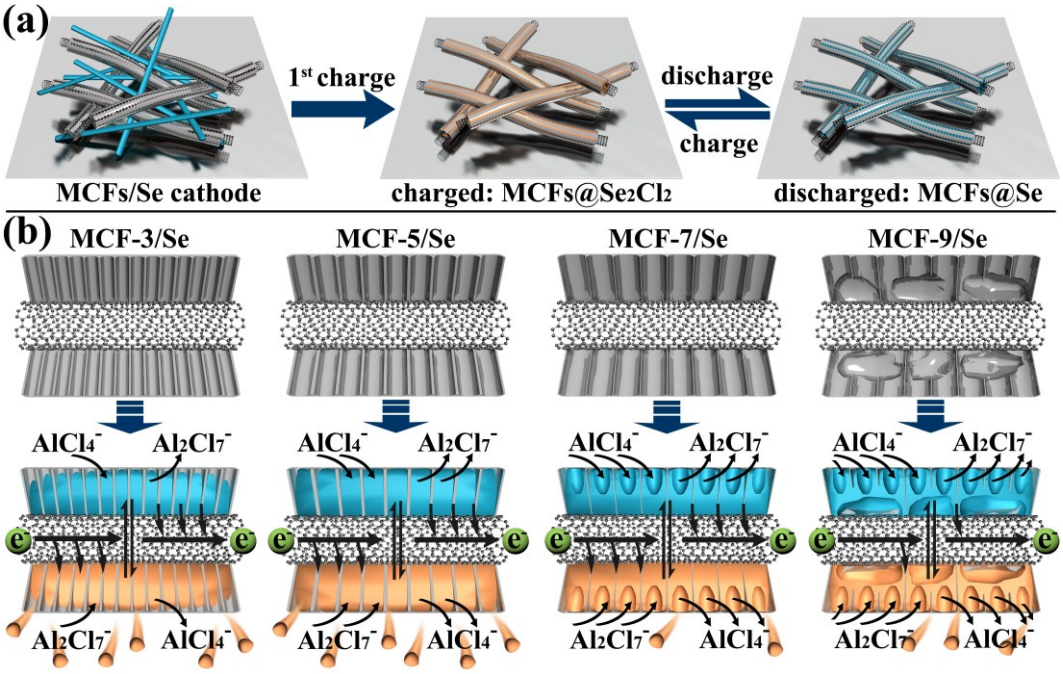

Figure 1. Schematic illustrations of (a) electrochemical processes of MCFs/Se cathodes in Al-Se batteries, and (b) the mesopore size dependent ion diffusivity of chloroaluminate anions and the impact of mesoporous carbon shell and CNT core interconnection on electrode conductivity.

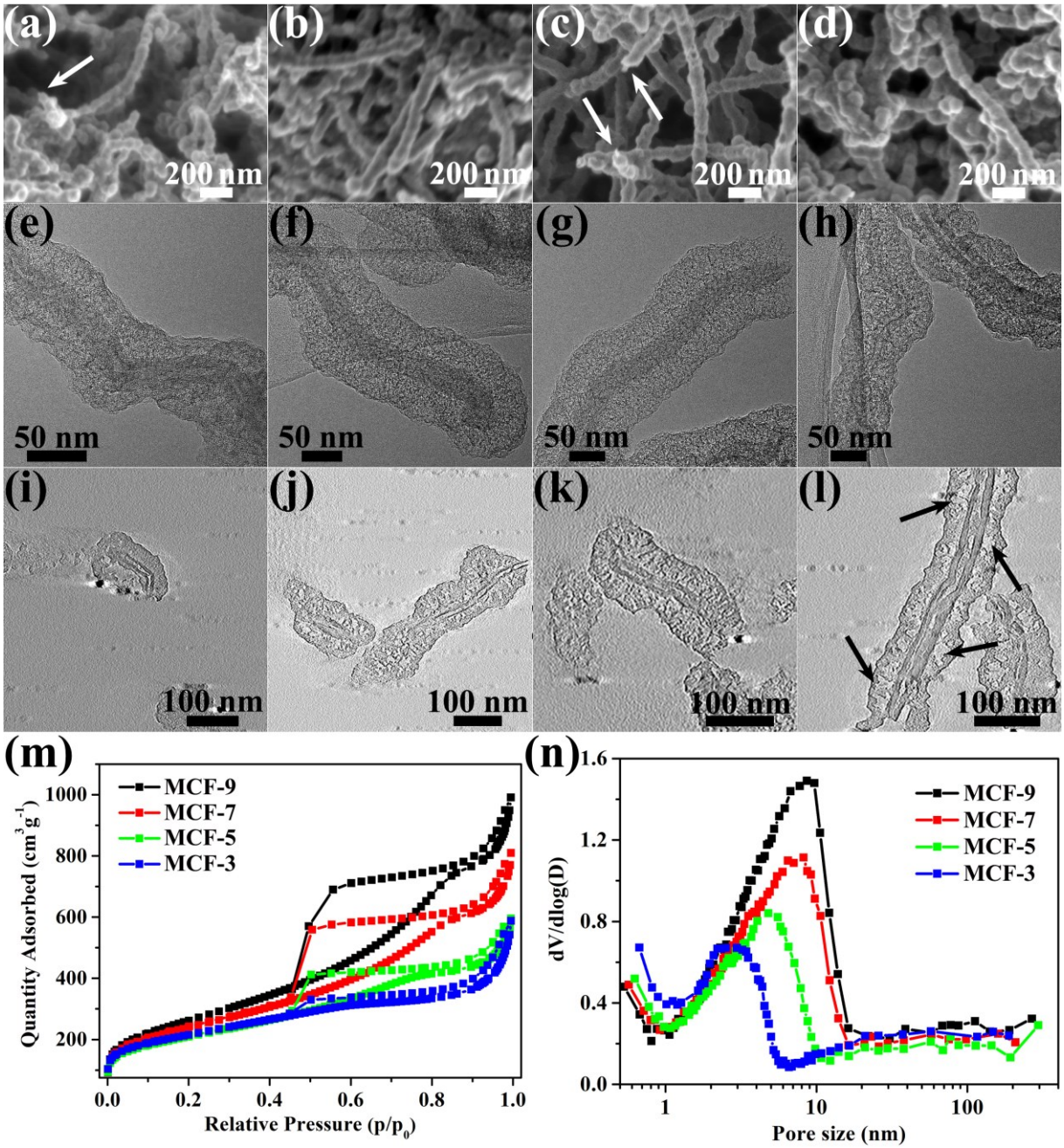

Figure 2. Structural characterizations of MCFs. (a-d) Typical SEM images of MCF-3, MCF-5, MCF-7 and MCF-9. (e-h) TEM images of MCF-3, MCF-5, MCF-7 and MCF-9. (i-l) ET slides cutting from the middle of MCF-3, MCF-5, MCF-7 and MCF-9 single fiber. (m) Nitrogen adsorption/desorption isotherms and (n) the pore size distributions of MCFs.

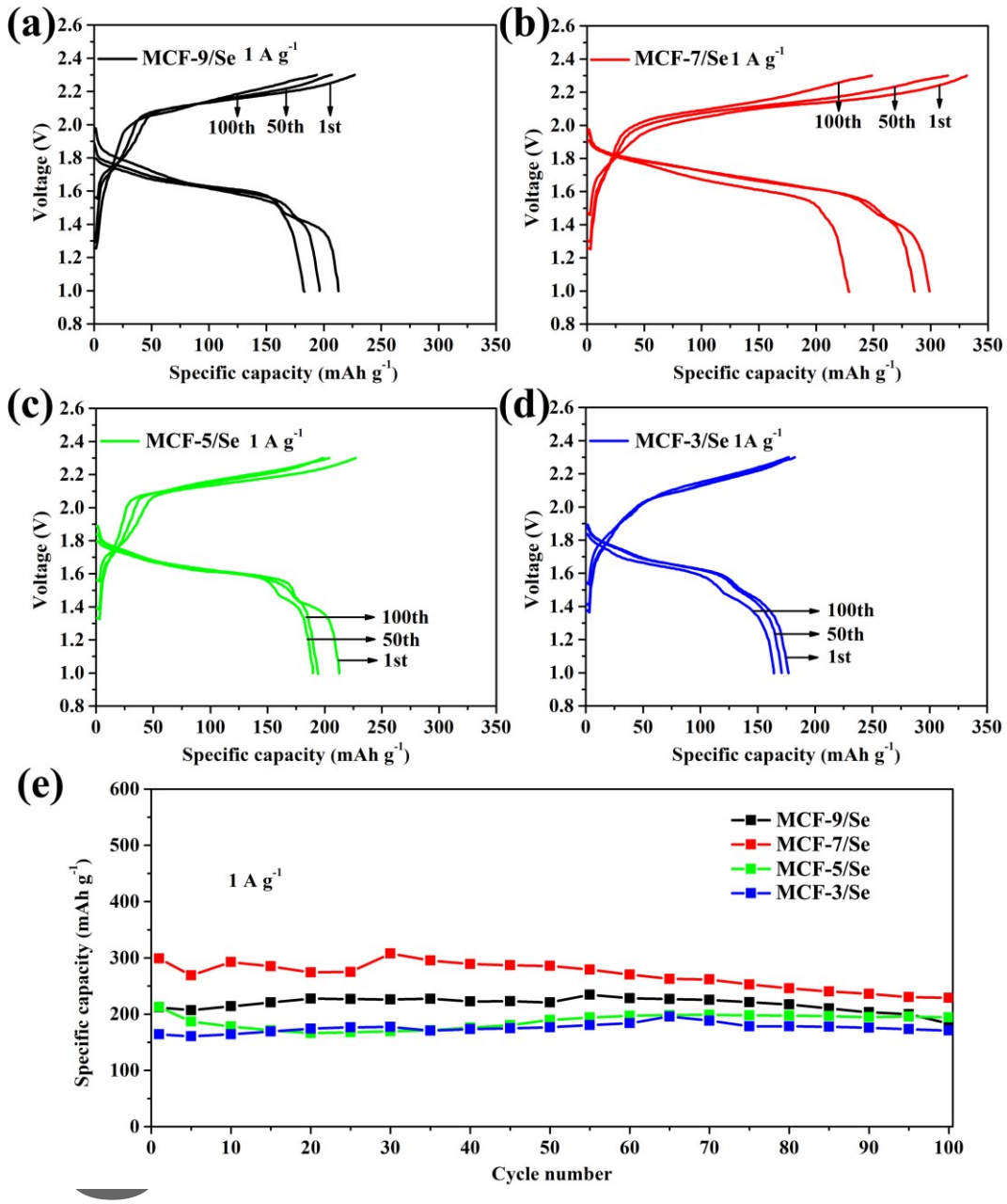

Figure 3. Galvanostatic charge/discharge measurements of MCFs/Se composite cathodes at 1A g^{-1} in Al-Se batteries. (a-d) The charge/discharge profiles of MCF-9/Se, MCF-7/Se, MCF-5/Se and MCF-3/Se. (e) The cycling performances of MCFs/Se cathodes.

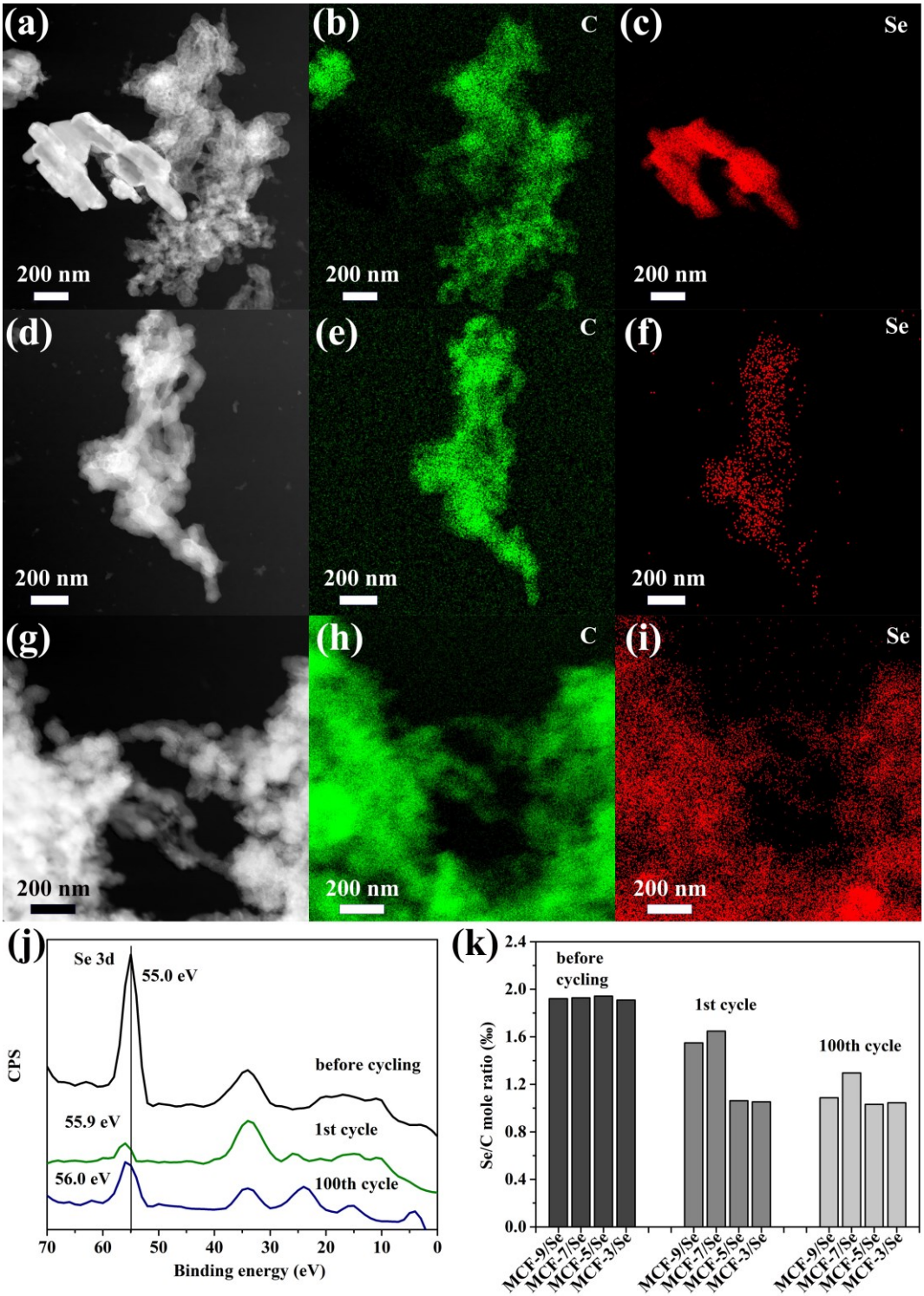

Figure 4. TEM elemental mapping images of MCF-7/Se cathode before battery test (a-c), after 1st cycle (d-f) and after 100th cycle (g-i) at 1 A g^{-1}. (j) Se high resolution XPS analysis of MCF-7/Se cathode at different testing cycles at 1 A g^{-1}. (k) The relative Se content analysis of MCFs/Se cathodes.

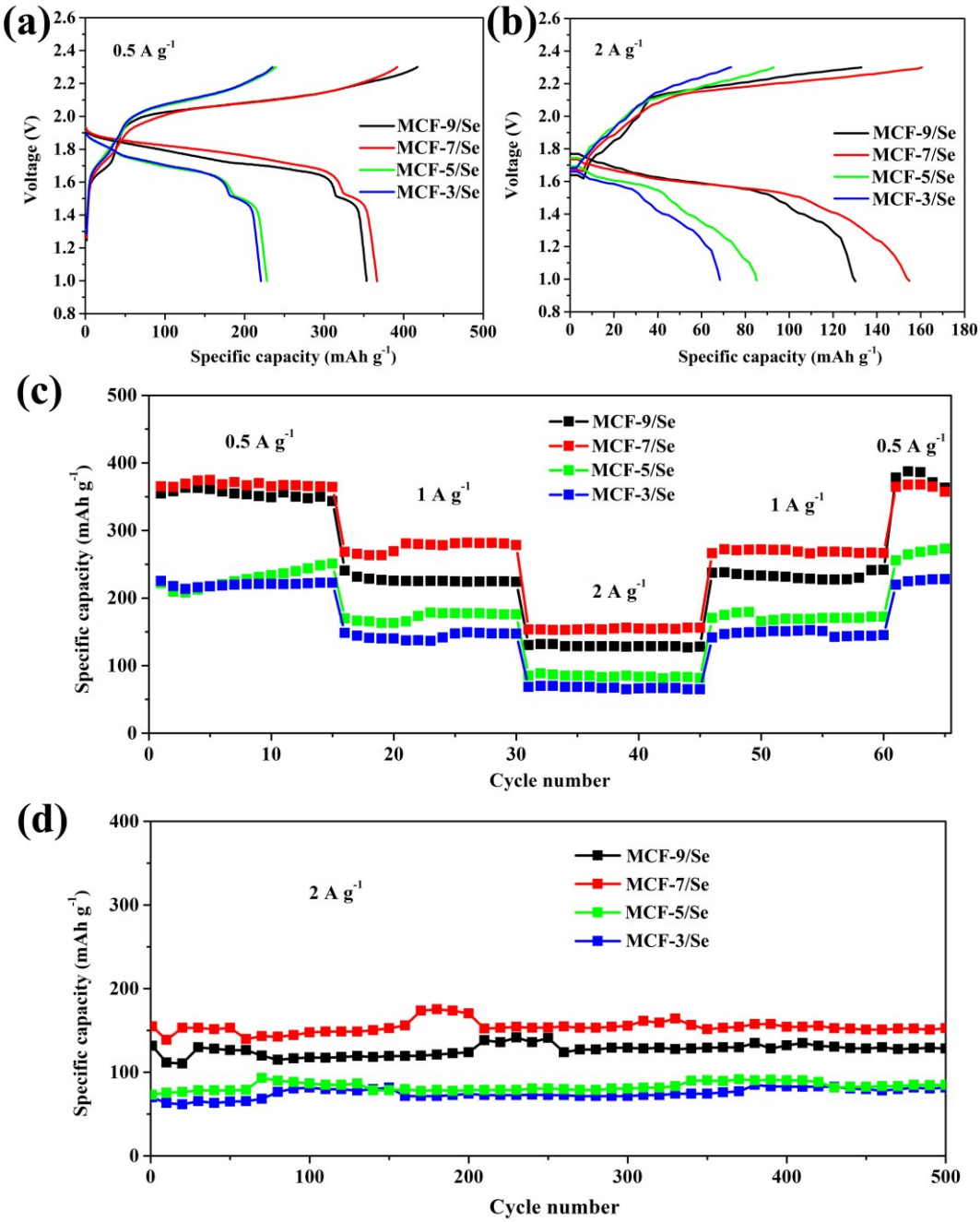

Figure 5. The rate and long cycling performances of MCFs/Se cathodes in Al-Se batteries. (a-b) Typical charge/discharge profiles of MCFs/Se cathodes at 0.5 and 2 A g^{-1}. (c) The rate capacities of MCFs/Se cathodes. (d) Long cycling performances of MCFs/Se at 2 A g^{-1}.

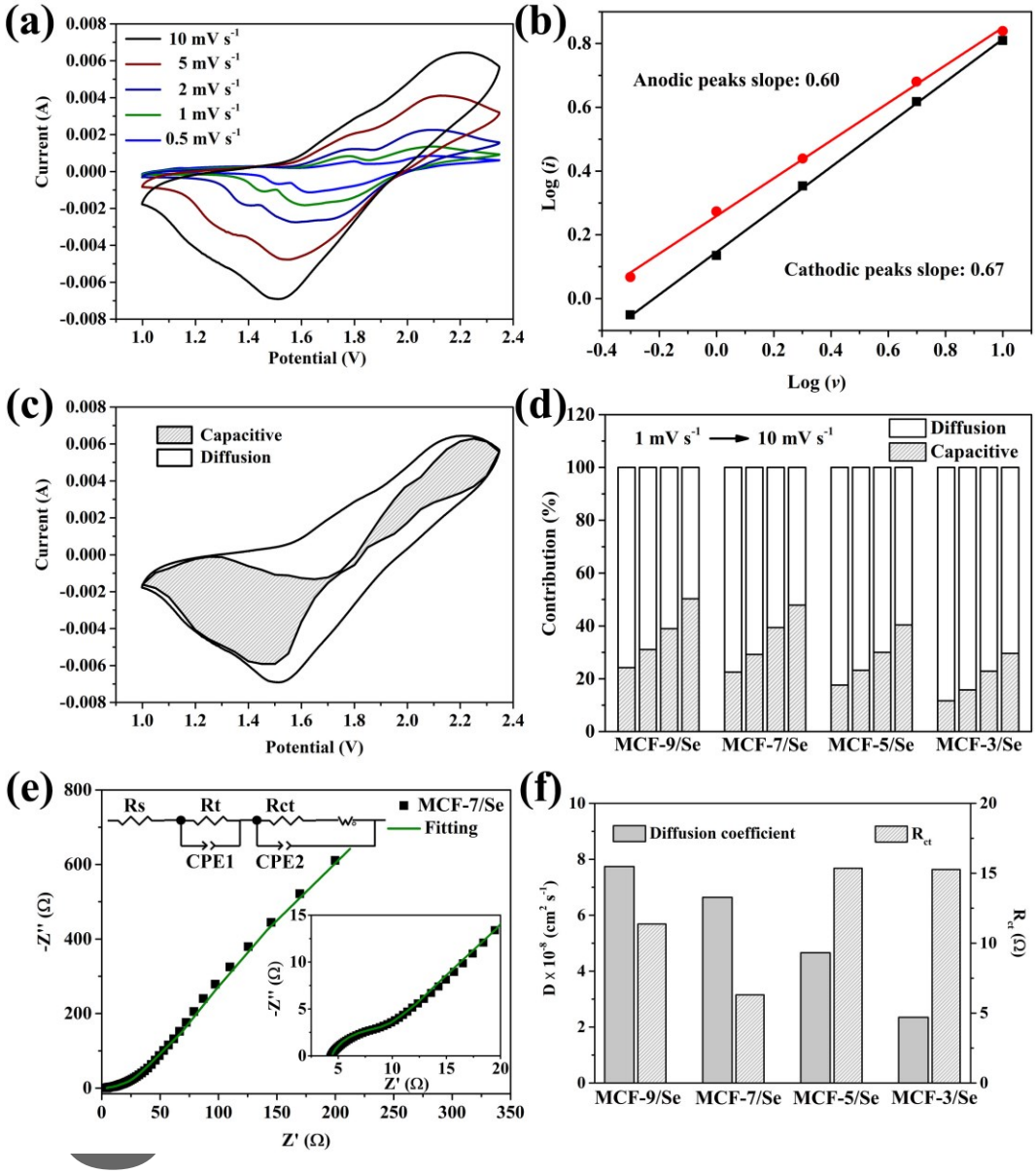

Figure 6. Electrochemical analysis of MCFs/Se cathodes in Al-Se batteries. (a) CV curves of MCF-7/Se recorded at scan rates of 0.5, 1, 2, 5 and 10 mV s^{-1}. (b) The log (*i*)-log(*v*) plots of both anodic and cathodic peaks and their linear fitting results. (c) Capacitive and diffusion contribution of MCF-7/Se cathode at 10 mV s^{-1}. (d) Contribution proportion of diffusion and capacitive processes of MCFs/Se cathodes at different scan rates. (e) Nyquist plot of MCF-7/Se (inset: the magnified high frequency region) and the equivalent circuit fitting. (f) Charge transfer resistance (R_{ct}) and ion diffusion coefficients (D) calculated from EIS.

Mesoporous carbon fibers (MCFs) with finely modulated ion diffusion property and electrochemical conductivity have been developed for high performance Al-Se batteries. These materials are synthesized by coaxially coating mesoporous carbon with tunable mesopore sizes on carbon nanotubes. The trade-off between electrolyte ion diffusivity and electrode conductivity determines MCF with 7.1 nm pores as the best host material for Al-Se batteries.

Keyword: rechargeable aluminium batteries, mesoporous carbon, selenium cathode, ion diffusivity, electrode conductivity

Yueqi Kong, Ashok Kumar Nanjundan, Yang Liu, Hao Song, Xiaodan Huang* and Chengzhong Yu*

Modulating Ion Diffusivity and Electrode Conductivity of Carbon Nanotube@Mesoporous Carbon Fibers for High Performance Aluminium-Selenium Batteries